

Scaled-up aqueous redox flow battery using anthraquinone negalyte and vanadium posilyte with inorganic additive

Gyunho Park^a, Hayoung Jeong^b, Wonmi Lee^a, Jeong Woo Han^{b,**}, Duck Rye Chang^{c,**}, Yongchai Kwon^{a,d,*}

^a Graduate School of Energy and Environment, Seoul National University of Science and Technology, 232 Gongneung-ro, Nowon-gu, Seoul 01811, Republic of Korea

^b Department of Materials Science and Engineering, Research Institute of Advanced Materials, Seoul National University, 1 Gwanak-ro, Gwanak-gu, Seoul 08826, Republic of Korea

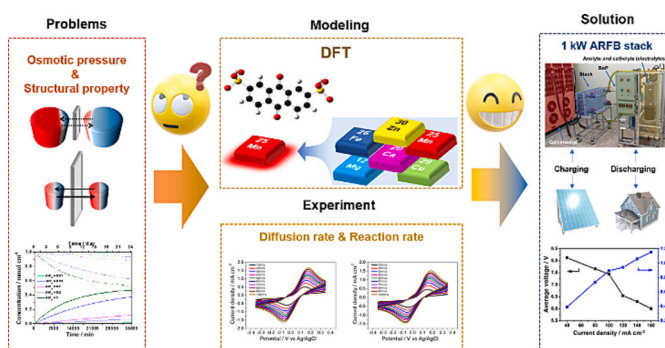
^c Gwangju Research Center, Korea Institute of Industrial Technology, Gwangju 506-824, Republic of Korea

^d Department of Chemical and Biomolecular Engineering, Seoul National University of Science and Technology, 232 Gongneung-ro, Nowon-gu, Seoul 01811, Republic of Korea

HIGHLIGHTS

- ARFB stack using 2,7-AQDS and VOSO₄ as redox couple is achieved.
- MnSO₄ additive is imported to suppress crossover of VOSO₄.
- Ratio of area to electrolyte volume determines crossover rate in ARFB systems.
- In ARFB single cell, capacity retention rate increases from 82 to 88% at 80 mA·cm⁻².
- In ARFB stack, a high power of 1.15 kW is achieved at 160 mA·cm⁻².

GRAPHICAL ABSTRACT



ARTICLE INFO

Keywords:

Anthraquinone-2,7-disulfonic acid
Vanadium oxide sulfate
Manganese sulfate
One kW aqueous redox flow battery stack
Cycle stability

ABSTRACT

In this study, one kilowatt aqueous redox flow battery (ARFB) using anthraquinone-2,7-disulfonic acid (2,7-AQDS) and vanadium oxide sulfate (VOSO₄) as active materials for negalyte (negative electrolyte) and posilyte (positive electrolyte) is successfully accomplished. Then, manganese sulfate (MnSO₄) is further included in negalyte to increase reactivity of active materials and to suppress their crossover by controlling their osmotic pressure. This binary effects of MnSO₄ are predicted by density functional theory and reduction in concentration gap. The decrease in energy band gap of 2,7-AQDS with MnSO₄ facilitated electron transfer rate. Anodic and cathodic diffusion coefficient and reaction rate constant are also improved. More specifically, with adoption of MnSO₄ additive, energy efficiency and capacity retention rate of ARFB single cells operated with MnSO₄ additive are improved from 79.1 to 83.9% at the current density of 40 mA cm⁻² and from 82 to 88% at the current density

* Corresponding author at: Department of Chemical and Biomolecular Engineering, Seoul National University of Science and Technology, Republic of Korea

** Corresponding authors: Gwangju Research Center, Korea Institute of Industrial Technology, Gwangju 506-824, Republic of Korea; Department of Materials Science and Engineering, Research Institute of Advanced Materials, Seoul National University, 1 Gwanak-ro, Gwanak-gu, Seoul 08826, Republic of Korea

E-mail addresses: jwhan98@snu.ac.kr (J.W. Han), drchang@kitech.re.kr (D.R. Chang), kwon@seoultech.ac.kr (Y. Kwon).

<https://doi.org/10.1016/j.apenergy.2023.122171>

Received 18 July 2023; Received in revised form 29 September 2023; Accepted 23 October 2023

Available online 2 November 2023

0306-2619/© 2023 Elsevier Ltd. All rights reserved.

of 80 mA cm^{-2} after 100 cycles. Based on that, ARFB stack using 2,7-AQDS and VO_2 with MnSO_4 additive is prepared and this ARFB stack exhibits a high power of 1.15 kW.

1. Introduction

The amount of fossil fuel consumption increases as demands for energy consumption grow. However, these fossil fuels can be depleted, while they accelerate global warming with the significant emission of carbon dioxide [1–5]. To overcome these issues, renewable energies, such as solar and wind power, have received much attention. However, the development of proper energy storage systems (ESSs) becomes required because these renewable energies are produced intermittently and irregularly [6–10]. Among these ESSs, redox flow batteries (RFBs) have edges regarding scalability and geological dependency because they can install power and capacity sectors independently by controlling the area of electrodes and the volume of tanks. Furthermore, RFBs can produce relatively higher efficiency than other competitive energy storage systems [11–15].

Aqueous redox flow batteries (ARFBs) that are operated in water-based electrolytes have better advantages than non-aqueous redox flow batteries (NARFBs) because organic solvents used in NARFBs are usually explosive and volatile [16–21]. Additionally, ARFBs can work even at high current density ranges due to high ionic conductivity of

aqueous electrolytes. Simultaneously, they have excellent advantages in terms of cost and environmental friendliness [20,22].

Vanadium redox flow batteries (VRFBs), which contain vanadium ions in both electrolytes, have been considered [23–27]. Compared with other RFB systems, in VRFBs, the cross-contamination of vanadium ions is considerably suppressed because the same vanadium ions are used as redox active materials in both electrolytes. Furthermore, VRFBs usually show a long lifespan over 20 years, and high chemical stability. Accordingly, VRFBs were widely explored from fundamental study to practical applications [12,28–31], while VRFB systems of kW ~ MW level were fabricated [32,33].

However, the redox reaction of vanadium ions is related to only one electron, and therefore, their energy density is lower than that of other active materials whose redox reactions involved two electrons [34–37]. Furthermore, VRFBs have very confined operational temperature range, and this weakens their stability and induces the precipitation of vanadium ions during the operation of VRFBs. The expensive cost of vanadium also retards the commercialization of VRFBs.

In this prospect, organic materials can replace vanadium because their cost can be considerably reduced through bulk production

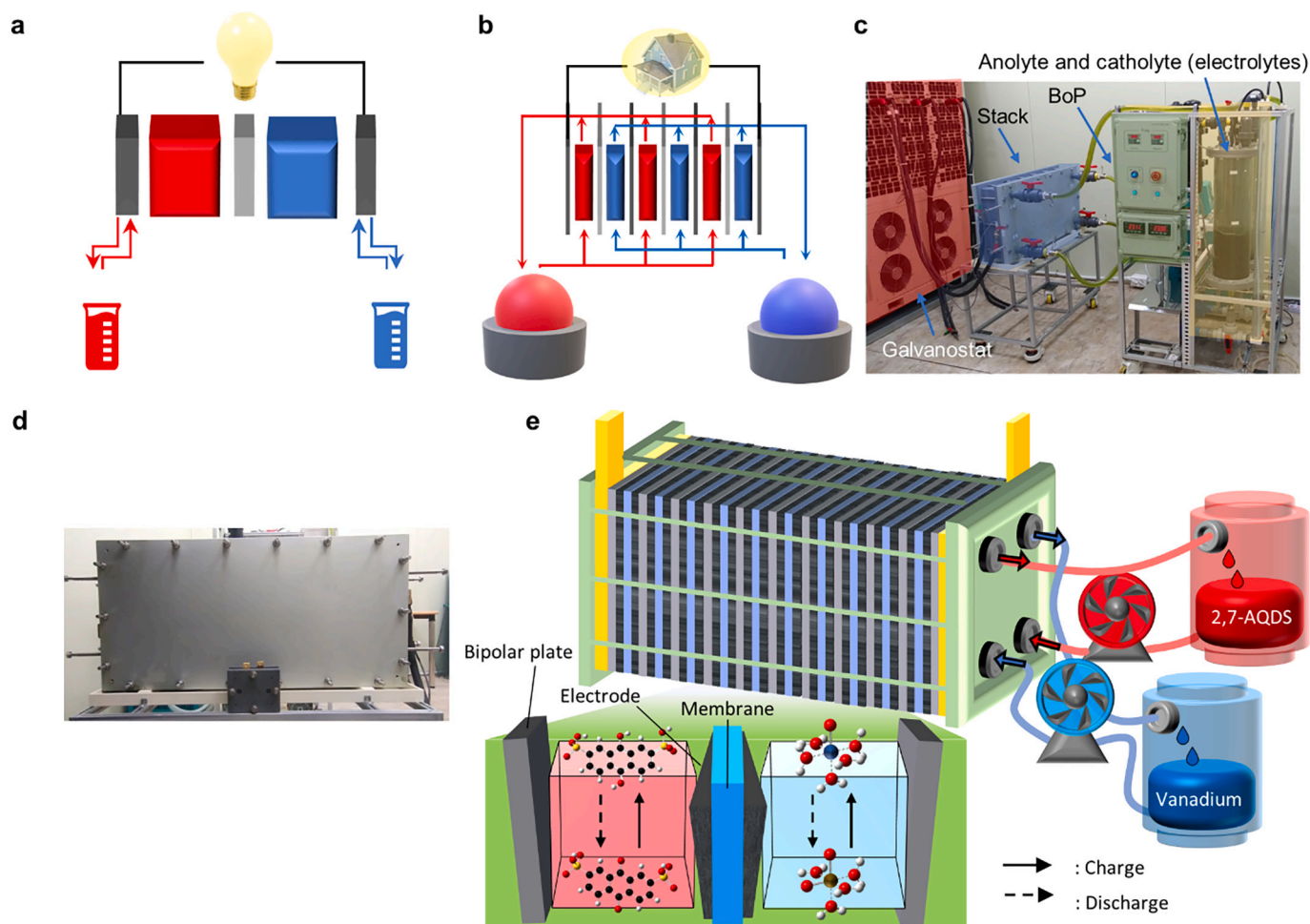


Fig. 1. Schematic illustrations and digital images of the ARFB. (a) ARFB single cell configured by assembling bipolar plates, electrodes, and a membrane and (b) ARFB stack containing large reservoirs for both negalyte and posilyte. (c) The overall components fabricated for evaluating the cycle performance of 1 kW class ARFB stack. Here, galvanostat, ARFB stack, balance of plant (BoP), and electrolytes were the main components. (d) Photo images of ARFB single cell including the active area of 25 cm^2 and ARFB stack including the total active area of 1200 cm^2 . (e) An overall schematic diagram of ARFB stack.

[38–42]. Furthermore, their excellent flexibility in redox potential and solubility by importing appropriate functional groups are their another merit [43–45]. As a previous study, Huskinson et al. suggested ARFB single cell using 9,10-anthraquinone-2,7-disulphonic acid (2,7-AQDS) and Br_2 as redox couple, and the ARFB reached 0.6 W cm^{-2} at 1.3 A cm^{-2} with good capacity retention [46]. However, the use of toxic Br_2 is problem.

Although kW-class ARFB systems using vanadium were established in ESS market, those using organic materials have not been reported yet [47–49]. Thus, in this study, for the first time, 1 kW ARFB stack system using anthraquinone-2,7-disulphonic acid (2,7-AQDS) and vanadium oxide sulfate (VOSO_4) is suggested. Compared with VRFBs, the cost of negalyte is considerably saved by replacing expensive vanadium with cheap 2,7-AQDS [46]. The related discussion is listed in **Supplementary Note 1** of supplementary information (SI). Instead of toxic Br_2 , well-established positive vanadium is used for posilyte. For the fabrication of ARFB stack, several ARFB single cells are connected in series (Fig. 1 (a) and (b)). while additional balance of plant is also required to complete the entire ARFB stack system (Fig. 1(c) and (d)). Its schematic diagram is represented in Fig. 1(e).

Besides that, manganese sulfate (MnSO_4), which is a cheap inorganic material, is used not only to enhance the capacity retention by suppressing the crossover of vanadium cations, but also to increase the energy efficiency (EE) of ARFB by improving the redox kinetics of 2,7-AQDS. The improved capacity retention of ARFBs using MnSO_4 additive are explained by the concepts of reduced osmotic pressure. Strong interaction between active site of 2,7-AQDS and MnSO_4 additive results in advanced redox reaction kinetics. These predictions are confirmed by density functional theory (DFT) based computational method and electrochemical experiments.

2. Experimental section

2.1. Materials

Anthraquinone-2,7-disulfonic acid disodium salt (purity of 80%) was purchased from Career Henan Chemical Co. and vanadium oxide sulfate (VOSO_4) (purity of 72.64%) was purchased from Shinko Chemical Co., Ltd. Manganese sulfate (MnSO_4 , anhydrous, purity of 99.5%), ammonium chloride (NH_4Cl , purity of 99.0%) and sulfuric acid (H_2SO_4 , purity of 95%) were purchased from Samchun Chemicals. Especially, sodium ions in anthraquinone-2,7-disulfonic acid disodium salt were replaced with proton ions by using the same resin process that was applied in previous studies [20,50]. This exchanged material was denoted as anthraquinone-2,7-disulfonic acid (2,7-AQDS).

2.2. Cyclic voltammetry (CV)

To evaluate the electrochemical properties and OCV of active materials used in ARFB single cell test, cyclic voltammetry (CV) tests were performed by using a potentiostat (SP-240, BioLogic). A glassy carbon electrode (GCE, 5 mm in diameter) and/or carbon felt (SGL Carbon Group, Germany) were used as working electrode. Pt wire and Ag/AgCl electrodes were used as counter and reference electrode, respectively. Here, the reference electrode was soaked in 3 M NaCl solution before the tests. The size of carbon felt considered as the working electrode for CV tests was $2 \text{ cm} \times 1 \text{ cm}$. The volume of electrolytes was 20 mL and scan rate range was from 10 mV s^{-1} to 100 mV s^{-1} .

2.3. ARFB single cell test

To examine the effect of MnSO_4 additive on the performance of ARFB single cell, cycle tests were carried out by using charge-discharge equipment (Wonatech, WBCS3000). 40 mL of 3 M H_2SO_4 solution containing 0.25 M 2,7-AQDS and 0.25 M MnSO_4 or only 0.25 M 2,7-AQDS was used as negalyte, while 40 mL of 3 M H_2SO_4 solution containing 0.5

M VOSO_4 and 2 M NH_4Cl was used as posilyte. The electrode area was $5 \text{ cm} \times 5 \text{ cm}$ (25 cm^2), and Nafion 115 membrane was used as the separator. A peristaltic pump (EMP-2000 W, EMS tech) equipped with pump head in 2-Channels (Masterflex) was used for the test, while the flow rate was controlled to 25 mL min^{-1} . The cut-off voltage range for ARFB single cell tests was from 0.2 to 1.4 V. N_2 gas was purged for 5 min before the tests. Furthermore, to analyze the cross-contamination of active materials after cycling test, the solutions were examined by UV–vis spectrometry (Backman, DU640).

2.4. 1 kW scale ARFB stack test

To evaluate the performance of 1 kW ARFB stack, 14 L of 3 M H_2SO_4 solution containing 0.25 M 2,7-AQDS and 0.25 M MnSO_4 was used as negalyte, while 0.5 M VOSO_4 and 2 M NH_4Cl were dissolved in 14 L of 3 M H_2SO_4 solution as posilyte. Carbon felts of 1200 cm^2 size and Nafion 115 membranes were used in ARFB stack system that was formed by a serial connection of ten AFB single cells. The flow rate of electrolytes was 1200 mL min^{-1} . To get carbon felts wet, the inlet point of electrolytes was positioned at the lower part of cell, while their outlet point was positioned at the diagonal upper part of cell. The temperature of electrolytes remained stably at 30°C through the cooler. The cut-off voltage range of ARFB stack was from 2 to 14 V.

2.5. DFT calculation

To compare the band gap between 2,7-AQDS when MnSO_4 was dissolved and when it was not, density functional theory (DFT) calculations were performed using the Jaguar software. (SCHRÖDINGER, Inc.) Conformational analysis was conducted by Conformational Search tool from the Jaguar MacroModel package with OPLS-2005 force field. The most stable structures were selected as the initial structures and their further optimizations were performed using the optimization tool in the Jaguar software. The B3LYP-D3 hybrid DFT method and the basis set of 6-31G** were used. Energy convergence was set to energy change $< 5 \times 10^{-5}$ Hartree, and root mean square (RMS) density matrix change $< 5 \times 10^{-6}$ Hartree. PBF solvent model was used in the solvent calculation, and dielectric constant, molecular weight, density were set to describe the probe radius of solvent molecule. In addition, molecular orbitals were calculated in Optimization property tools to evaluate each band gap.

3. Results and discussion

3.1. Investigation on a ratio of reaction area to volume of cell configuration

When ARFBs are operated, the crossover of active materials through membrane is a big problem because this may induce low coulombic efficiency (CE) and rapid capacity decay of ARFBs. Under the hypothesis that crossover is mainly originated from diffusion mechanism, the crossover issue can be alleviated by optimizing the structural property of ARFB cell system. In this prospect, a ratio of reaction area to volume can be the critical property to reduce the crossover. For exploring the effect of this ratio on the crossover of active materials, the following permeability equations are suggested [51].

$$V_P \frac{dC_P(t)}{dt} = A \frac{P}{L} (C_N(t) - C_P(t)) \quad (1)$$

$$C_N(t) + C_P(t) = C_{total} \quad (2)$$

where V_P is the volume of pure solution without active materials, C_P is the concentration of active materials measured in pure solution, C_N is the concentration of active materials measured in their concentrated side, C_{total} is the total concentration of active materials contained in both

electrolytes, A and L are the area and thickness of membrane, and P is the permeability coefficient of active materials permeated through membrane. When the crossover of active materials occurs, C_N is reduced, whereas C_P increases.

Based on Eq. (1), the permeability coefficient of active materials is calculated by a slope of linear line derived from a correlation of the concentration of active material contained in the pure solution side and the elapsed time. The corresponding correlation is expressed as below.

$$\frac{dC_P(t)}{dt} = \frac{PA}{LV_P} (C_N(t) - C_P(t)) \quad (3)$$

Here, $C_P(t)$ and $C_N(t)$ are expressed as Eqs. (4) and (5) by a combination of Eqs. (2) and (3). The detailed calculation process is explained in SI.

$$C_P(t) = \frac{C_{total}}{2} \left(1 - \exp\left(-2 \frac{PA}{LV_P} t\right) \right) \quad (4)$$

$$C_N(t) = C_{total} - C_P(t) = \frac{C_{total}}{2} \left(1 + \exp\left(-2 \frac{PA}{LV_P} t\right) \right) \quad (5)$$

According to Eq. (4), as $\frac{A}{V_P}$ increases, C_P increases more rapidly over time. This means that when the area of membrane, A , is large and the volume of reservoir, V_P , is small, C_N becomes rapidly reduced. With the input of various $\frac{A}{V_P}$, concentration profiles measured with elapsed time are plotted in Fig. 2(a). More specifically, C_{total} , P and L are assumed as reasonable ones for VRFB with Nafion 212 membrane from references [52–54]. They are 1 mmol cm^{-3} , $2 \times 10^{-7} \text{ cm}^2 \text{ min}^{-1}$ and 0.005 cm , respectively. Solid and dot lines mean C_P and C_N . As shown in Fig. 2(b) and (c), ARFB system operated in low $\frac{A}{V_P}$ keeps the concentration of active material more stable than that operated in high $\frac{A}{V_P}$ during the same time period. When this concept is considered, A , V_P , and $\frac{A}{V_P}$ in ARFB single cell and stack are summarized in Table 1.

According to Table 1, the decrease in concentration of active

Table 1

Comparison of $\frac{A}{V_P}$ in ARFB single cell and ARFB stack.

Type	A / cm^2	V_P / L	$\frac{A}{V_P} / \text{cm}^{-1}$
ARFB single cell	25	0.04	0.625
ARFB stack	1200×10	14	0.857

material is higher in ARFB stack than in ARFB single cell because $\frac{A}{V_P}$ in ARFB stack is higher than that in ARFB single cell. This may induce lower CE and worse cycle stability in ARFB stack than in ARFB single cell due to a higher crossover of active materials occurring at ARFB stack. Furthermore, although a better output power can be achieved by enlarging the area of electrode in ARFB stack, the crossover of active materials through membrane may increase due to the mismatch between the storage tank volume of ARFB stack and its electrode area. This implies that the design of ARFB stack increasing power by enlarging the electrode area may be in a trouble due to the increased crossover of active materials and the decrease in CE and EE of ARFB stack.

One strategy to suppress the crossover of active materials is to use electrochemically inactive additive in electrolyte. Regarding electrolyte, optimizing its composition is very critical to increase the performance and stability of ARFB stack, although the migration of electrolyte is a natural phenomenon occurring over the operation of ARFB. Actually, redox-active materials solvated with water molecules tend to be transferred from one side to the opposite side by water migration in the aqueous phase. Because of that, when the composition of electrolytes is unbalanced, the crossover of redox-active materials increases, while their redox reactivity is weakened, and eventually, ARFB using the electrolytes becomes unstable. To alleviate the water migration issue, diminishing the osmotic pressure gap of two electrolytes (negalyte and posilyte) by further inclusion of additive is important [55,56].

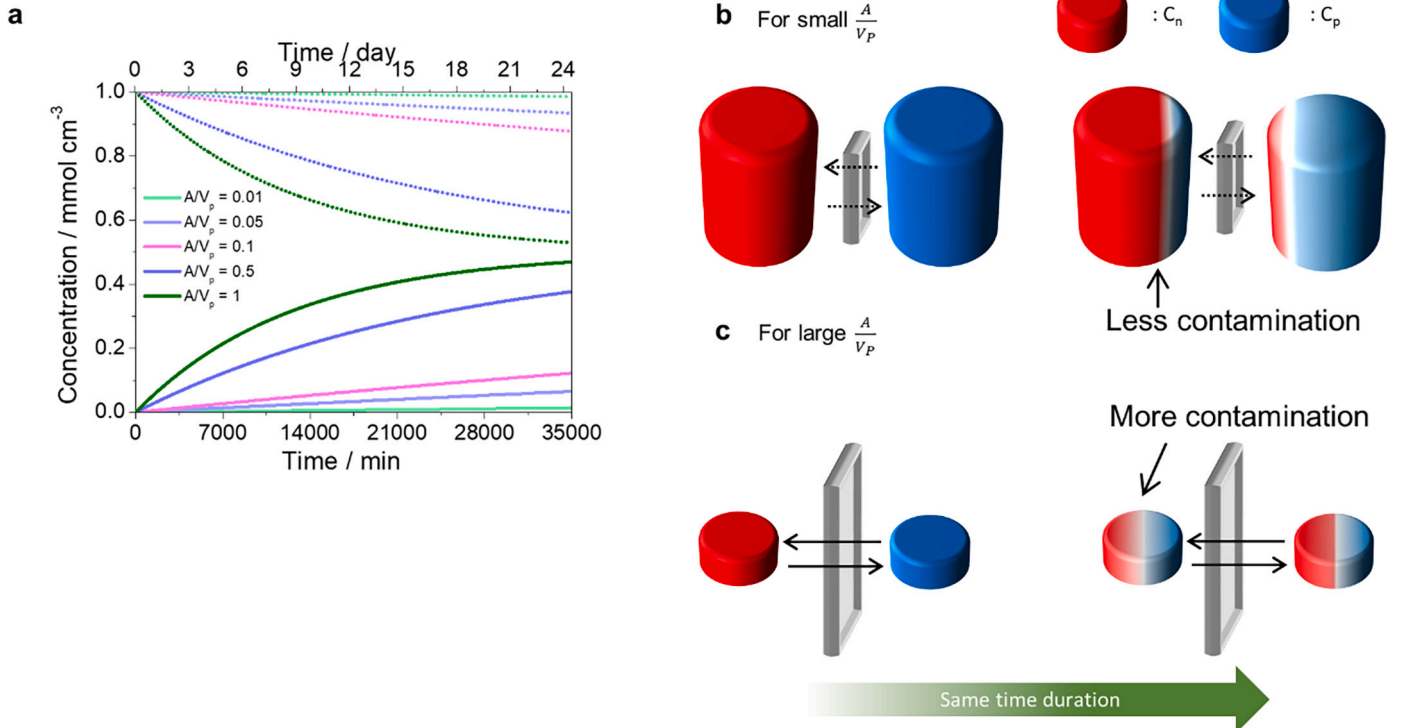


Fig. 2. Relation between reaction area (A) and electrolyte volume (V_P). (a) Concentration distributions of active materials calculated in conditions of (b) low $\frac{A}{V_P}$ and (c) high $\frac{A}{V_P}$.

3.2. Selection of promising additive and its effect on electrolyte

To predict the optimal condition of proper additive determining the properties of electrolyte, density functional theory (DFT) calculation was adopted. Furthermore, there were some previous studies that considered the effects of additives for optimizing the properties of electrolyte and suppressing the crossover of active materials, although they were mostly related to VRFBs. According to their VRFB studies, the composition of electrolyte determined the solvation structure of vanadium ions, their crossover, and the migration of water [37,57,58]. In this aspect, NH_4^+ ions were a famous additive because they could suppress the precipitation of V_2O_5 species due to steric hindrance and coulombic repulsion between cations [58]. In addition, Cl^- ions could form soluble VO_2Cl species with VO_2^+ ions in a mixed sulfate-chloride solution [37].

With the above examples, in this RFB system, NH_4Cl is considered as additive for posilyte to suppress the side reaction of vanadium ions. Likewise, for negalyte, an inorganic additive is applied to promote the complexation of the electron structure of 2,7-AQDS molecules, and enhance their chemical stability and redox reactivity. For the purpose, various dications including Mn^{2+} , Mg^{2+} , Fe^{2+} , Zn^{2+} and Ca^{2+} were regarded as the additive candidate, and their interaction energy with 2,7-AQDS molecules was calculated by DFT. According to DFT calculation, these dications strongly interacted with oxygen atoms attached to carbonyl groups included in 2,7-AQDS molecules, while the oxygen atoms acted as the active sites for redox reaction of quinone species. Of the dications, Mn^{2+} ions showed the strongest interaction with 2,7-AQDS molecules (Fig. 3(a)). Such a strong interaction by Mn^{2+} cations can fortify the complexation of electron structure of 2,7-AQDS molecules than that by other cations, and such strengthened complexation improves the redox reactivity of 2,7-AQDS molecules.

Since components of active material, supporting electrolyte and additive were recognized in both electrolytes, as a next sequence, the actual concentration of each component of both electrolytes was determined. The calculated concentrations of electrolytes are suggested in Fig. 3(b). Initially, in posilyte, the concentration of VOSO_4 , NH_4Cl , and H_2SO_4 was 0.5, 2.0, and 3.0 M, respectively, meaning that the total concentration of posilyte was 5.5 M. In contrast, in the prospect of dissociated ion, the total concentration of posilyte was 11 M (0.5 M VO^{2+} , 0.5 M SO_4^{2-} , 2.0 M NH_4^+ , 2.0 M Cl^- , 3.0 M H^+ and 3.0 M HSO_4^-).

Next, the effect of MnSO_4 additive on the crossover of water molecules is quantitatively evaluated. In negalyte, when MnSO_4 additive is not included, since the total concentration of negalyte (6.25 M) that consists of 0.25 M 2,7-AQDS, 3.0 M H^+ and 3.0 M HSO_4^- is lower than

that of posilyte (11 M), strong water migration may occur from negalyte to posilyte. In contrast, when MnSO_4 additive is included, the total concentration of negalyte increases to 6.75 M that is the sum of 0.25 M Mn^{2+} , 0.25 M SO_4^{2-} and the original 6.25 M negalyte. Thus, water migration from negalyte to posilyte may be alleviated due to the reduced osmotic pressure gap between negalyte and posilyte. To sum up, it is expected that the crossover of hydrated vanadium ions will be reduced by keeping the concentration of electrolytes in balance.

However, since the solubility of MnSO_4 in the mixture of 0.25 M 2,7-AQDS and 3.0 M H_2SO_4 is relatively low (< 0.5 M), the reduction in the osmotic pressure gap has limitation. To overcome the limitation of the low amount of dissolved MnSO_4 and to balance the ion concentration between negalyte and posilyte, the concentration of NH_4Cl included in posilyte should be well controlled. To sum up, MnSO_4 additive strongly interacts with 2,7-AQDS molecules, and the electrochemical kinetics of 2,7-AQDS molecules is improved. In addition, the migration of water or hydrated vanadium ions is alleviated by keeping the ion balance between negalyte and posilyte by optimizing the concentration of additives. Furthermore, such optimal concentration of additive will affect the suppression of migration of active materials in ARFB stack whose cross-contamination rate increases by its high $\frac{A}{V_p}$.

3.3. Evaluation of electrochemical characterization

To evaluate OCV of redox couple consisting of 2,7-AQDS and VOSO_4 and their electrochemical properties, CV curves were measured. Their redox reactions and electrochemical reactivity are presented in Fig. 4, while electrochemical parameters are summarized in Table 2. In 2,7-AQDS, the proton-coupled redox reaction including two protons and electrons occurs in acidic condition, while the redox reaction of hydrated vanadium ions accompanies only one electron. Consequently, two vanadium ions per one 2,7-AQDS molecule are required to keep the charge balance.

OCV was 1 V irrespective of the use of additive. Furthermore, the redox reaction of 2,7-AQDS was more reversible with higher I_{pa}/I_{pc} ratio than that of vanadium ions. Regarding additive effect, when MnSO_4 additive was included, ΔE_p of 2,7-AQDS was smaller than that measured without additive. The small ΔE_p means a fast electron transfer rate, and this may induce a low charge-discharge overpotential, followed by improved VE of ARFBs. These experimental results were verified by DFT calculations. In addition, as earlier mentioned, NH_4Cl was considered as additive for posilyte because this could prevent the precipitation of vanadium ions [50].

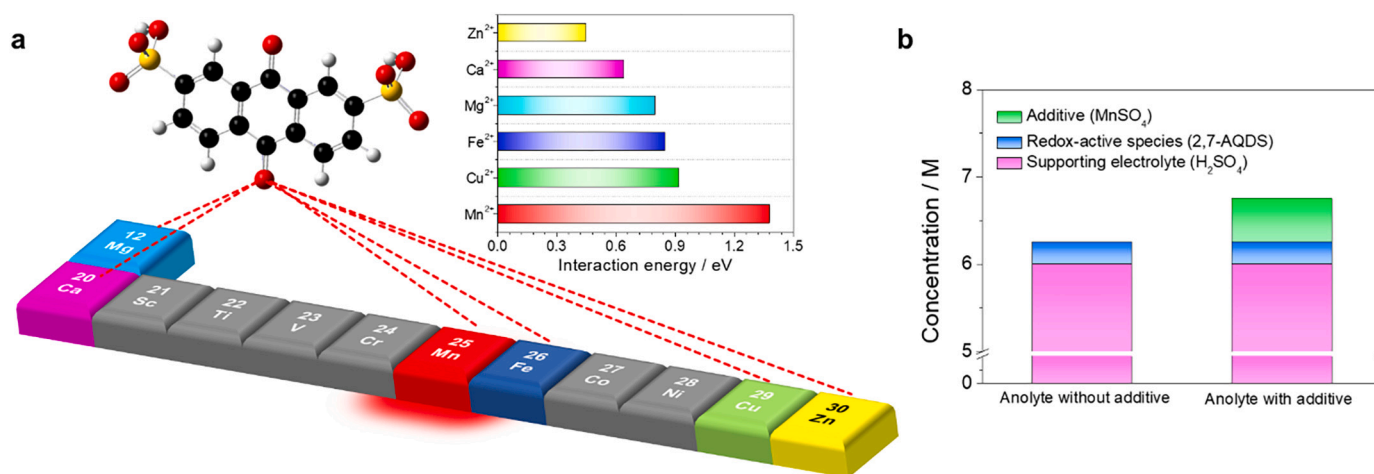


Fig. 3. Scanning of additive candidates and estimating electrolyte concentration. (a) Calculated interaction energies between 2,7-AQDS molecule and dications. (b) Calculated composition of negalyte including MnSO_4 additive and posilyte. The composition of negalyte without MnSO_4 additive is 0.25 M 2,7-AQDS and 3.0 M H_2SO_4 . The composition of negalyte including MnSO_4 additive is 0.25 M 2,7-AQDS, 0.25 M MnSO_4 and 3.0 M H_2SO_4 , while that of posilyte is 0.5 M VOSO_4 and 2.0 M NH_4Cl and 3.0 M H_2SO_4 .

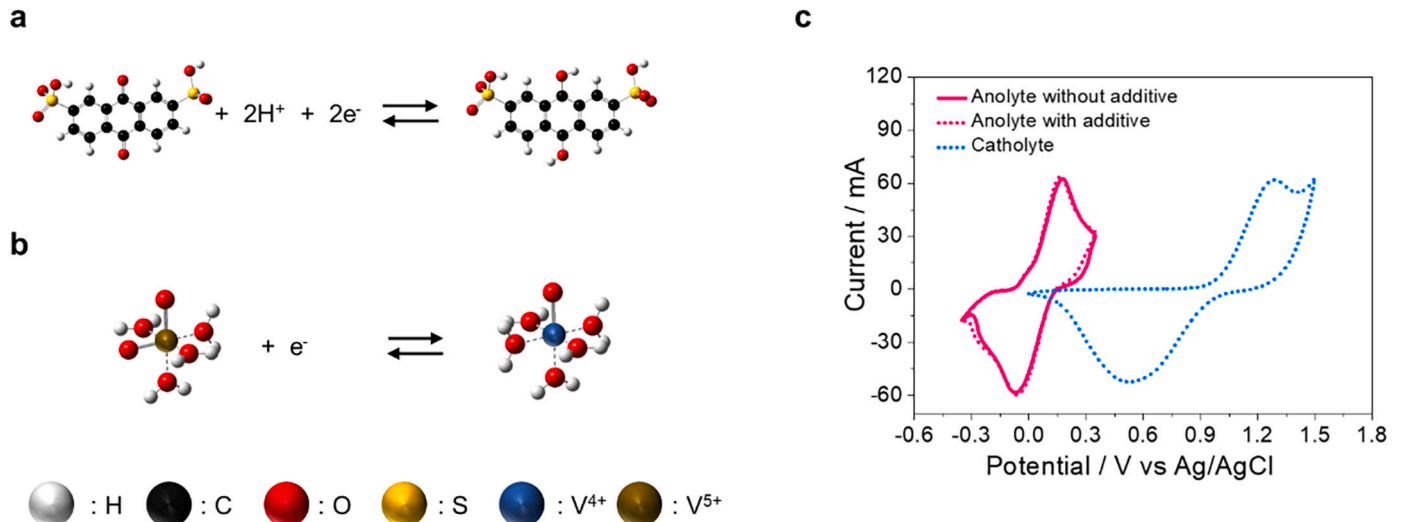


Fig. 4. Redox reactions of active materials cycle voltammetry (CV). The redox reactions of (a) 2,7-AQDS and (b) vanadium ions (V^{4+}/V^{5+}). (c) CV curves of 12.5 mM 2,7-AQDS and 25 mM $VOSO_4$ dissolved in 3.0 M H_2SO_4 as negalyte and posilyte using carbon felt as working electrode. 12.5 mM $MnSO_4$ was further included to negalyte as additive. The scan rate was 20 mV s^{-1} .

Table 2

Electrochemical parameters of electrolytes evaluated by the measurements of CV curves.

Electrolytes	ΔE_p (V)	I_{pa} (mA cm^{-2})	I_{pc} (mA cm^{-2})	I_{pa}/I_{pc}
Negalyte without additive	0.25	62.27	-58.30	1.07
Negalyte with additive	0.23	64.10	-59.41	1.08
Posilyte	0.76	61.81	-52.35	1.18

To measure kinetic parameters of 2,7-AQDS, its peak current density and peak potential separation with and without $MnSO_4$ additive are measured (Fig. S1(a) and (b)). As shown in Fig. S1(c) and (d), a relation between peak current density and the square root of scan rate was evaluated with different scan rates ($10\text{--}100 \text{ mV s}^{-1}$) to calculate diffusion coefficient of negalyte. The corresponding linear curve was observed, and the diffusion coefficient was calculated by Randle-Sevcik's equation for irreversible reaction.

$$i_p = 2.99 \times 10^5 n^{3/2} \alpha^{1/2} c D_0 \nu^{1/2} \quad (6)$$

where i_p refers to the peak current density (mA cm^{-2}), n is the number of electrons transferred in the redox reaction (in this case, n is two), α is charge transfer coefficient which can be estimated from $|E_p - E_{p/2}| = (48/\alpha n) \text{ mV}$, where E_p and $E_{p/2}$ mean the potential at peak current density and the half potential of peak current density, c refers to the concentration of active material (mol L^{-1}), D_0 ($\text{cm}^2 \text{ s}^{-1}$) is the diffusion coefficient of the active material and ν (V s^{-1}) is scan rate [59].

According to Randle-Sevcik's equation for irreversible reaction, D_a (anodic diffusion coefficient) and D_c (cathodic diffusion coefficient) of negalyte including $MnSO_4$ additive were 2.26×10^{-7} and $1.97 \times 10^{-7} \text{ cm}^2 \text{ s}^{-1}$. In contrast, those of negalyte measured without additive were 1.84×10^{-7} and $1.48 \times 10^{-7} \text{ cm}^2 \text{ s}^{-1}$. With this result, this is recognized that $MnSO_4$ used as additive of negalyte can enhance the diffusion coefficient of 2,7-AQDS. The improvement in diffusion coefficient indicates that 2,7-AQDS molecules are well transferred to electrode, and this further induces the reduction in overpotential and the improvement in efficiencies of ARFBs.

In addition, to calculate standard rate constant (k_0), the following equation was used.

$$i_p = 0.227 F A k_0 c \times \exp\left(\frac{\alpha F}{RT} (E_p - E^0)\right) \quad (7)$$

$$E^0 = \frac{E_{pa} + E_{pc}}{2} \quad (8)$$

where the difference between peak potential (E_p) and formal electrode potential (E^0) was measured from CV curves. E^0 was determined as the average of anodic peak potential (E_{pa}) and cathodic peak potential (E_{pc}). The plot of natural logarithm of cathodic peak current ($\ln(i_{pc})$) versus ($E_p - E^0$) produces a linear relationship and standard rate constant (k_0) is derived from the intercept of y-axis. n was defined in Eq. (3), R refers to the universal gas constant ($8.314 \text{ J K}^{-1} \text{ mol}^{-1}$), T is the absolute temperature (298.15 K), F is faraday constant ($96,485 \text{ C mol}^{-1}$).

Standard rate constants (k_0) were calculated by the relation between $\ln(i_{pc})$ and corresponding ($E_p - E^0$) (Fig. S1(e) and (f)). k_0 of negalyte including $MnSO_4$ additive was $5.73 \times 10^{-5} \text{ cm s}^{-1}$, which was higher than that measured without additive ($4.91 \times 10^{-5} \text{ cm s}^{-1}$). The increase in k_0 means that its electron transfer resistance is reduced and VE of ARFB increases.

With the estimated D and k_0 , it is substantiated that $MnSO_4$ molecules provided to an equimolar amount of 2,7-AQDS molecules play a role in improving the redox reactivity and electron transfer rate of 2,7-AQDS. To support the experimental results, energy band gap of both oxidized and reduced 2,7-AQDS is expected by DFT calculations (Fig. 5). In H_2SO_4 environment, both forms of 2,7-AQDS containing $MnSO_4$ additive have a lower energy band gap than those without additive. The energy band gaps in 2,7-AQDSs was calculated without H_2SO_4 in Fig. S2. This indicates that $MnSO_4$ additive affects the reduction in energy band gap of 2,7-AQDS regardless of the inclusion of H_2SO_4 , and this leads to a fast electron transfer rate, followed by an excellent redox reactivity of 2,7-AQDS.

3.4. The performance evaluations of ARFB single cells

The discharge capacity of ARFB single cell measured during 300 cycles with and without $MnSO_4$ additive is presented in Fig. 6(a). The capacity utilization ratio of ARFB single cell measured with $MnSO_4$ additive was higher than that measured without additive over the total time period. A higher capacity utilization was due to enhanced diffusion coefficient of 2,7-AQDS by the adoption of $MnSO_4$ additive. With the improved diffusion behavior, 2,7-AQDS molecules can be easily accessible to the surface of electrode, resulting in a higher discharge capacity of ARFB single cell. In addition, as shown in Fig. 6(b), VE and EE of ARFB single cell measured with $MnSO_4$ additive were better than those

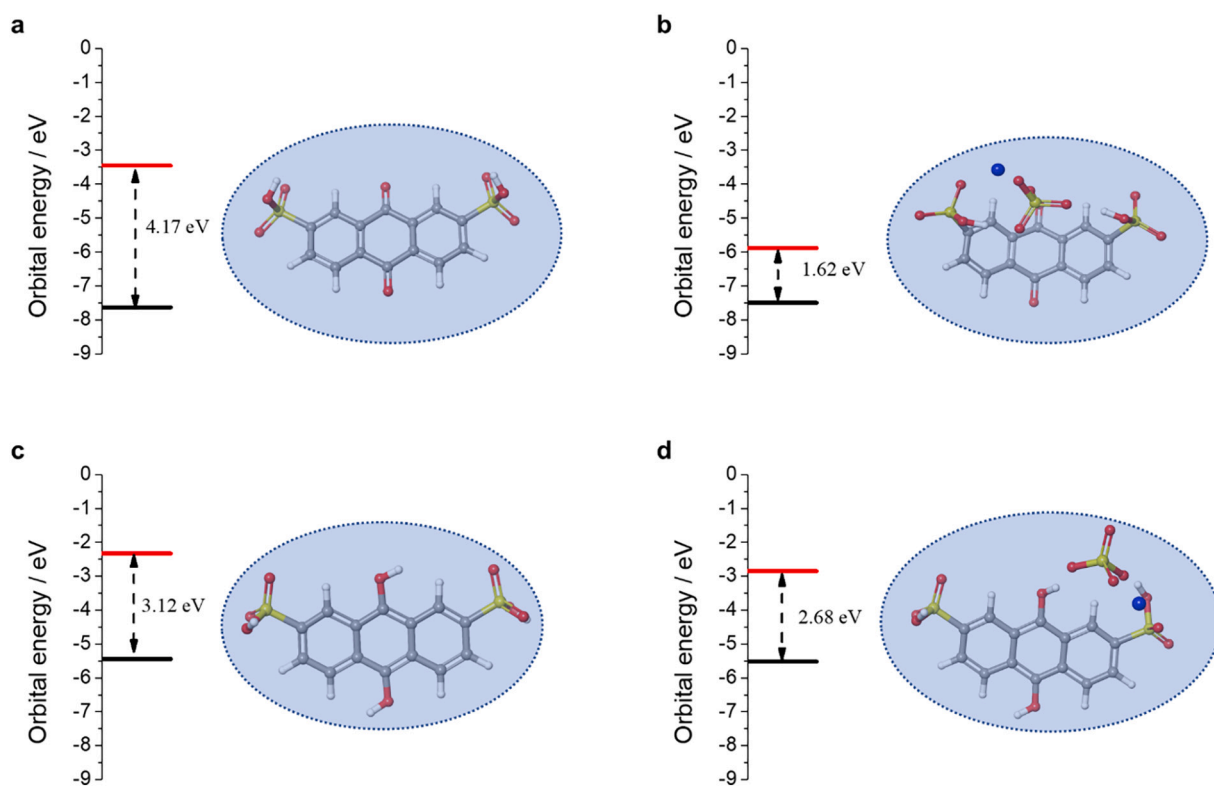


Fig. 5. Energy band gap of both oxidized and reduced 2,7-AQDS dissolved in supporting electrolyte. Energy band gap of (a) oxidized 2,7-AQDS and (c) reduced 2,7-AQDS calculated without additive. (b) Oxidized 2,7-AQDS and (d) reduced 2,7-AQDS calculated with additive. The blue background means supporting electrolyte environment (H₂SO₄). The blue ball refers to Mn²⁺ ion, and it is assumed that MnSO₄ additive is included in equimolar with 2,7-AQDS. (For interpretation of the references to colour in this figure legend, the reader is referred to the web version of this article.)

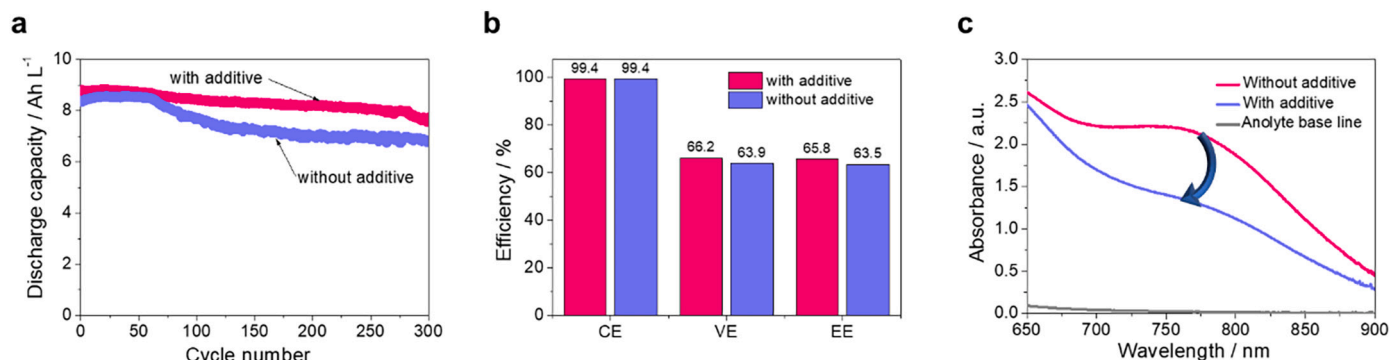


Fig. 6. ARFB single cell performance with and without additive. (a) Discharge capacity graphs of ARFB single cells measured with MnSO₄ additive and without the additive. (b) CE, VE and EE of the ARFB single cells. (c) Absorption spectrum of negalyte measured after ARFB single cell test. The ARFB single cell test was operated under 80 mA cm⁻².

measured without additive by 2.3%. This is due to the electron transfer rate of 2,7-AQDS improved by MnSO₄ additive. Consequently, it was confirmed that both efficiencies and discharge capacity utilization were improved in ARFB single cells when MnSO₄ additive was used.

As earlier expected, capacity decay in this ARFB system is mainly ascribed to the crossover of vanadium ions, which can permeate cation exchange membrane. When MnSO₄ additive was used, discharge capacity retention was 88% during 300 cycles (Fig. 6(a)), and this was higher than that measured without additive (82%). This is due to the reduced crossover of vanadium ions by the adoption of inorganic MnSO₄ additive. The UV–vis spectroscopic measurements of negalyte samples are shown in Fig. 6(c). Here, the negalyte samples were prepared after ARFB single cell tests performed with and without MnSO₄ additive. According to Fig. 6(c), the absorbance peak of V⁴⁺ ions that is supposed

to be observed at 765 nm was identified by adjusting the detecting range of UV–vis spectrometer without further dilution due to their low concentration. This indicated that when MnSO₄ additive was used, the concentration of vanadium ions contained in negalyte was lower than that measured without additive, showing that the crossover of vanadium ions was alleviated by MnSO₄ additive. More specifically, the crossover rate of vanadium ions was reduced up to about 60% by MnSO₄ additive, and this was well matched with Fig. 6(a). According to Fig. 6(a), capacity loss was reduced from 18 to 12% when MnSO₄ additive was used, meaning that the ratio of capacity loss rate between “with MnSO₄ additive” and “without additive” states was 66% (12/18 × 100%). This verifies that the capacity loss (66%) is closely linked to the crossover rate of vanadium ions (60%) and the low crossover of vanadium ions is due to the reduction in osmotic pressure gap, which is because the

concentration gap between negalyte and posilyte is reduced by further inclusion of MnSO_4 additive.

3.5. Comparison in performances of ARFB single cell and ARFB stack

The consecutive cycle data of ARFB single cell and ARFB stack measured at 100 and 40 mA cm^{-2} are presented in Fig. 7. According to Fig. 7(a) and (c), the retention rate of discharge capacity in ARFB stack was 82% at 100th cycle, which was lower than that in ARFB single cell (90%). This is due to a higher $\frac{\Delta V}{V_p}$ in ARFB stack than in ARFB single cell as earlier explained. This indicates that the crossover of active materials in ARFB stack is higher than that in ARFB single cell. Fig. 7(e) also shows a lower CE in ARFB stack than in ARFB single cell.

In contrast to CE, EE of ARFB stack was higher than that of ARFB

single cell (Fig. 7(b) and (d)). This is because VE in ARFB stack was higher than that in ARFB single cell. This trend in VE is related to a flow rate of electrolyte per unit area. More specifically, the flow rate in ARFB stack was faster than that in ARFB single cell. In this state, when the flow rate increases, the mass transfer resistance of active materials is reduced, and this can cause the increase in VE of ARFBs [50]. By the trade-off in the trend of CE and VE, EE in ARFB single cell and ARFB stack was similar as 83.9 and 83.7% (Fig. 7(e)). Furthermore, EE of ARFB single cell including additive (83.9%) was higher than that of ARFB single cell measured without additive (79.1%) due to the improved electrochemical kinetic parameters of 2,7-AQDS by the adoption of MnSO_4 additive.

The voltage profiles, polarization curves and efficiency graphs of ARFB single cell and ARFB stack measured at various current densities as

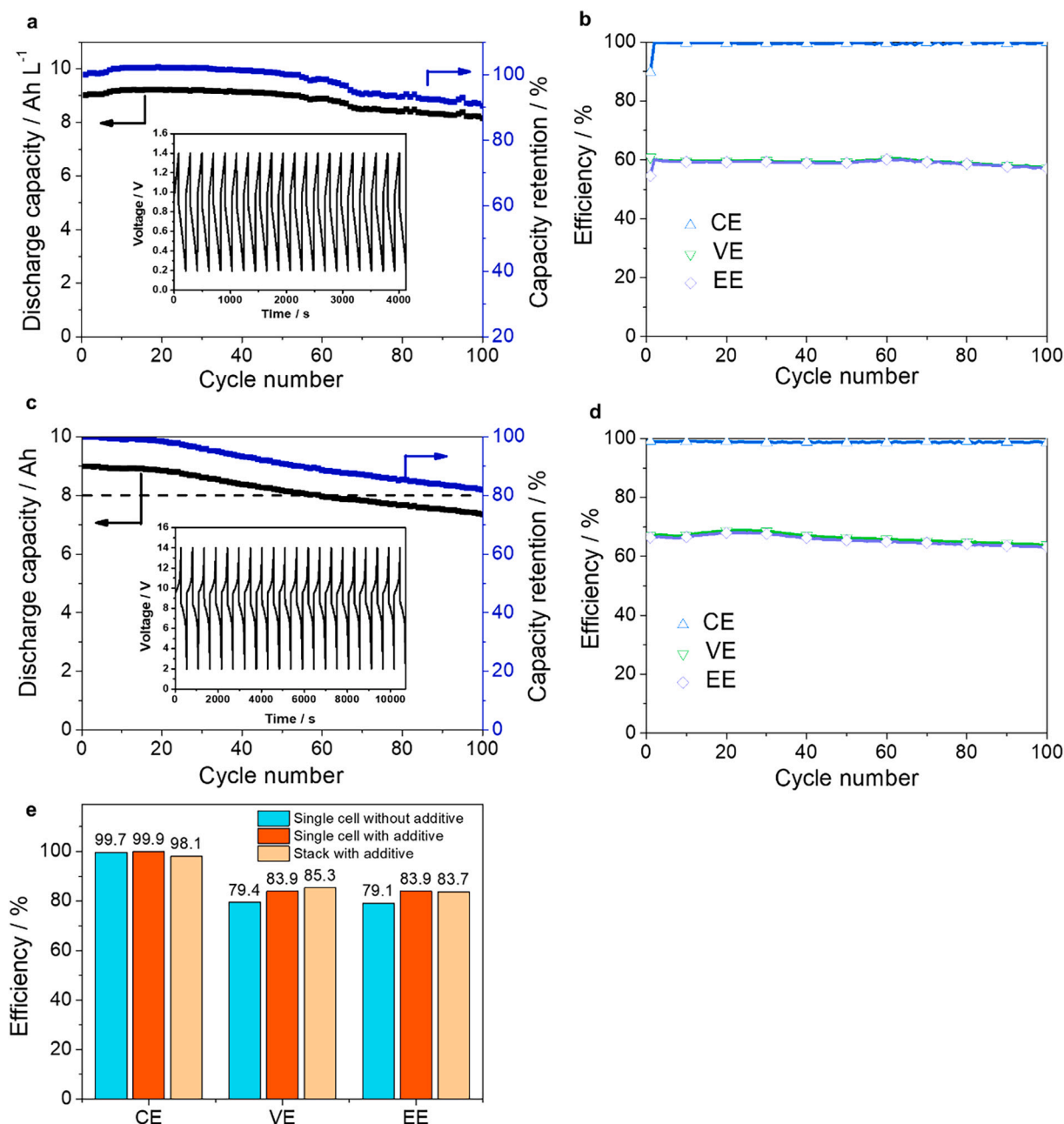


Fig. 7. Cycling data measured to compare the performances of ARFB single cell and ARFB stack. (a) Discharge capacity graph of ARFB single cell, and its inset showed the related voltage profile. (b) Efficiency graphs of ARFB single cell. (c) Discharge capacity graph of ARFB stack, and its inset showed the related voltage profile. (d) Efficiency graphs of ARFB stack. (e) Bar graphs representing efficiencies of ARFB single cells and ARFB stack using MnSO_4 additive in negalyte. The current density in (a) ~ (d) was 100 mA cm^{-2} while that in (e) was 40 mA cm^{-2} .

rate performance test data are shown in Fig. 8 and Fig. S3. Ohmic behavior was observed with linearly decreasing discharge voltage, which occurs due to the change in ohmic resistance. The voltage measured in ARFB stack was ten times higher than that measured in ARFB single cell. This is because ARFB stack was fabricated by the serial connection of ten ARFB single cells. According to Fig. 8(d), the power of ARFB stack was recorded as 1.15 kW at 160 mA cm^{-2} . However, in this configuration, its EE dramatically decreased as current density increased. VE of ARFB stack was 54% at 140 mA cm^{-2} , while that of ARFB single cell was about 51% at 160 mA cm^{-2} (Fig. S3). This means that applied current density should be lowered to achieve high EE, because ohmic resistance is the major resistance in these given current density ranges, whereas current should increase to obtain high power of ARFB stack. To meet the above targets of high EE and power, enlarging the area of electrode for ARFB stack is required. However, when enlarging the area of electrode is excessively increased, its imbalance with the volume of storage tank may induce a low CE of ARFB stack. It is therefore important to determine optimal $\frac{A}{V_p}$, to establish excellent ARFB stack.

4. Conclusions

1 kW level ARFB stack using 2,7-AQDS and VOSO_4 as active materials for negalyte and posilyte was accomplished. For doing that, additive candidates were considered to increase reactivity of active materials and to suppress their crossover by controlling their osmotic pressure. Especially, the crossover was affected by $\frac{A}{V_p}$. When $\frac{A}{V_p}$ of ARFB single cell and stack was compared, that of ARFB stack was 1.4 times higher than in ARFB single cell. Thus, when ARFB was scaled up, the compositions of electrolytes should be controlled by employing an appropriate additive to suppress crossover. As the additive, MnSO_4 was selected, and this helped to enhance the redox reactivity of 2,7-AQDS, which was

predicted by DFT calculation in advance. According to DFT calculation, the energy band gap of 2,7-AQDS was reduced with MnSO_4 additive (from 4.17 eV to 1.62 eV in oxidized form and from 3.12 eV to 2.68 eV in reduced form). This was because MnSO_4 additive had a strong interaction with active sites of 2,7-AQDS molecules. As a result, the electron transfer and diffusion coefficient of 2,7-AQDS were enhanced. With the benefits, EE of ARFB single cell including additive increased by 4.8% at 40 mA cm^{-2} , while its discharge capacity retention increased by 6% at 80 mA cm^{-2} . In current density step tests, ARFB stack showed the power of 1.15 kW at 160 mA cm^{-2} , and this is the world record of ARFB stack using 2,7-AQDS as active material. This study provides inspiration on the relation between electrode area size and electrolyte tank volume, and additive for high efficiency and long cycle life ARFBs stack considered as practical applications in large-scale industries.

CRediT authorship contribution statement

Gyunho Park: Writing – original draft, Formal analysis, Data curation, Conceptualization. **Hayoung Jeong:** Formal analysis, Data curation. **Wonmi Lee:** Formal analysis, Data curation. **Jeong Woo Han:** Writing – review & editing, Funding acquisition, Conceptualization. **Duck Rye Chang:** Writing – review & editing, Data curation, Conceptualization. **Yongchai Kwon:** Writing – review & editing, Supervision, Resources, Project administration, Conceptualization.

Declaration of Competing Interest

The authors declare that they have no known competing financial interests or personal relationships that could have appeared to influence the work reported in this paper.

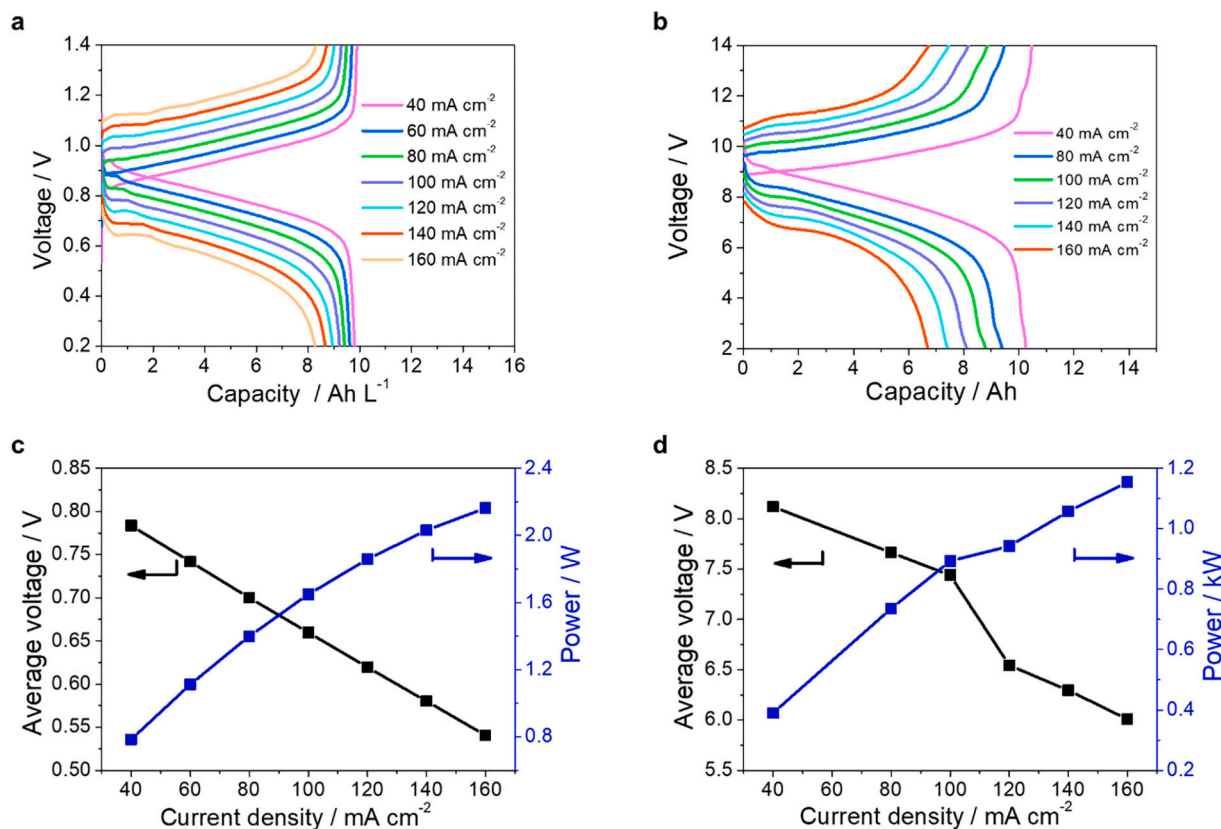


Fig. 8. Rate performance of ARFB single cell and stack. Voltage profiles of (a) ARFB single cell and (b) ARFB stack, and polarization curves of (c) ARFB single cell and (d) ARFB stack measured with various current densities.

Data availability

Data will be made available on request.

Acknowledgements

This research was financially supported by the Ministry of Trade, Industry and Energy (MOTIE) and Korea Institute for Advancement of Technology (KIAT) through the International Cooperative R&D Program (P0018437), Basic Science Research Program through the National Research Foundation of Korea (NRF) funded by the Ministry of Education (2021R1A6A1A03039981), the National Research Foundation of Korea (NRF) grant funded by the Korea Government. (MSIT) (2023R1A2C2002444) of the Republic of Korea.

Appendix A. Supplementary data

Supplementary data to this article can be found online at <https://doi.org/10.1016/j.apenergy.2023.122171>.

References

- Panja P. Deforestation, carbon dioxide increase in the atmosphere and global warming: a modelling study. *Int J Model Simul* 2021;41:209–19.
- Florides GA, Christodoulides P. Global warming and carbon dioxide through sciences. *Environ Int* 2009;35:390–401.
- Lashof DA, Ahuja DR. Relative contributions of greenhouse gas emissions to global warming. *Nature* 1990;344:529–31.
- Withey P, Johnston C, Guo J. Quantifying the global warming potential of carbon dioxide emissions from bioenergy with carbon capture and storage. *Renew Sustain Energy Rev* 2019;115:109408.
- Lin X, Zhu X, Han Y, Geng Z, Liu L. Economy and carbon dioxide emissions effects of energy structures in the world: evidence based on SBM-DEA model. *Sci Total Environ* 2020;729:138947.
- Kim JQ, So S, Kim H-T, Choi SQ. Highly ordered ultrathin Perfluorinated sulfonic acid ionomer membranes for vanadium redox flow battery. *ACS Energy Lett* 2021; 6:184–92.
- Noh C, Chung Y, Kwon Y. Optimization of iron and cobalt based organometallic redox couples for long-term stable operation of aqueous organometallic redox flow batteries. *J Power Sources* 2021;495:229799.
- Wu W, Luo J, Wang F, Yuan B, Liu TL. A self-trapping, bipolar Viologen bromide electrolyte for redox flow batteries. *ACS Energy Lett* 2021;6:2891–7.
- Connolly D, Lund H, Mathiesen BV, Pican E, Leahy M. The technical and economic implications of integrating fluctuating renewable energy using energy storage. *Renew Energy* 2012;43:47–60.
- Wang C, Li X, Yu B, Wang Y, Yang Z, Wang H, et al. Molecular design of fused-ring phenazine derivatives for long-cycling alkaline redox flow batteries. *ACS Energy Lett* 2020;5:411–7. <https://doi.org/10.1021/acsenergylett.9b02676>.
- Shin M, Noh C, Chung Y, Kwon Y. All iron aqueous redox flow batteries using organometallic complexes consisting of iron and 3-[bis (2-hydroxyethyl)amino]-2-hydroxypropanesulfonic acid ligand and ferrocyanide as redox couple. *Chem Eng J* 2020;398:125631.
- Huang Z, Mu A, Wu L, Wang H, Zhang Y. Electrolyte flow optimization and performance metrics analysis of vanadium redox flow battery for large-scale stationary energy storage. *Int J Hydrogen Energy* 2021;46:31952–62.
- Gundlapalli R, Jayanti S. Case studies of operational failures of vanadium redox flow battery stacks, diagnoses and remedial actions. *J Energy Storage* 2021;33: 102078.
- Noh C, Moon S, Chung Y, Kwon Y. Chelating functional group attached to carbon nanotubes prepared for performance enhancement of vanadium redox flow battery. *J Mater Chem A* 2017;5:21334–42.
- Lee W, Park G, Schröder D, Kwon Y. Performance enhancement of alkaline organic redox flow battery using catalyst including titanium oxide and Ketjenblack. *Korean J Chem Eng* 2022;39:1624–31.
- Jin S, Jing Y, Kwabi DG, Ji Y, Tong L, De Porcellinis D, et al. A water-miscible Quinone flow battery with high volumetric capacity and energy density. *ACS Energy Lett* 2019;4:1342–8.
- Lee W, Permatasari A, Kwon BW, Kwon Y. Performance evaluation of aqueous organic redox flow battery using anthraquinone-2,7-disulfonic acid disodium salt and potassium iodide redox couple. *Chem Eng J* 2019;358:1438–45.
- Lee W, Park G, Chang D, Kwon Y. The effects of temperature and membrane thickness on the performance of aqueous alkaline redox flow batteries using naphthoquinone and ferrocyanide as redox couple. *Korean J Chem Eng* 2020;37: 2326–33.
- Borchers PS, Strumpf M, Friebe C, Nischang I, Hager MD, Elbert J, et al. Aqueous redox flow battery suitable for high temperature applications based on a tailor-made ferrocene copolymer. *Adv Energy Mater* 2020;10:2001825.
- Permatasari A, Lee W, Kwon Y. Performance improvement by novel activation process effect of aqueous organic redox flow battery using Tiron and anthraquinone-2,7-disulfonic acid redox couple. *Chem Eng J* 2020;383:123085.
- Wu M, Bahari M, Fell EM, Gordon RG, Aziz MJ. High-performance anthraquinone with potentially low cost for aqueous redox flow batteries. *J Mater Chem A* 2021;9: 26709–16.
- Liu T, Wei X, Nie Z, Sprengle V, Wang W. A Total organic aqueous redox flow battery employing a low cost and sustainable methyl Viologen Anolyte and 4-HO-TEMPO Catholyte. *Adv Energy Mater* 2016;6:1501449.
- Lee W, Jung M, Serhiichuk D, Noh C, Gupta G, Harms C, et al. Layered composite membranes based on porous PVDF coated with a thin, dense PBI layer for vanadium redox flow batteries. *J Membr Sci* 2019;591:117333.
- Lim H, Shin M, Noh C, Koo E, Kwon Y, Chung KY. Performance evaluation of aqueous all iron redox flow batteries using heat treated graphite felt electrode. *Korean J Chem Eng* 2022;39:3146–54.
- Parasuraman A, Menictas C, Skyllas-Kazacos M. Review of material research and development for vanadium redox flow battery applications. *Electrochim Acta* 2013;101:27–40.
- Skylas-Kazacos M, Cao L, Kazacos M, Kausar N, Mousa A. Vanadium electrolyte studies for the vanadium redox battery—a review. *ChemSusChem* 2016;9: 1521–43.
- Wei L, Fan XZ, Jiang HR, Liu K, Wu MC, Zhao TS. Enhanced cycle life of vanadium redox flow battery via a capacity and energy efficiency recovery method. *J Power Sources* 2020;478:228725.
- Trovò A, Alotto P, Giomo M, Moro F, Guarnieri M. A validated dynamical model of a kW-class vanadium redox flow battery. *Math Comput Simul* 2021;183:66–77.
- Gu F-C, Chen H-C. Modelling and control of vanadium redox flow battery for smoothing wind power fluctuation. *IET Renew Power Gener* 2021;15:3552–63.
- Dassisi M, Cozzolino G, Chimienti M, Rizzuti A, Mastrolilli P, L'Abbate P. Sustainability of vanadium redox-flow batteries: benchmarking electrolyte synthesis procedures. *Int J Hydrogen Energy* 2016;41:16477–88.
- Martin J, Schafner K, Turek T. Preparation of electrolyte for vanadium redox-flow batteries based on vanadium pentoxide. *Energy Technol* 2020;8:2000522.
- Guarnieri M, Trovò A, Marini G, Sutto A, Alotto P. High current polarization tests on a 9 kW vanadium redox flow battery. *J Power Sources* 2019;431:239–49.
- Kear G, Shah AA, Walsh FC. Development of the all-vanadium redox flow battery for energy storage: a review of technological, financial and policy aspects. *Int J Energy Res* 2012;36:1105–20.
- Yang B, Hooper-Burkhardt L, Krishnamoorthy S, Murali A, Prakash GKS, Narayanan SR. High-performance aqueous organic flow battery with Quinone-based redox couples at both electrodes. *J Electrochem Soc* 2016;163:A1442–9.
- Lee W, Park G, Kwon Y. Alkaline aqueous organic redox flow batteries of high energy and power densities using mixed naphthoquinone derivatives. *Chem Eng J* 2020;386:123985.
- Lee W, Park D, Park G, Chang D, Kwon Y. Effect of pore adjustable hydrophilic nickel coated polyethylene membrane on the performance of aqueous naphthoquinone based redox flow batteries. *Chem Eng J* 2021;408:127320.
- Li L, Kim S, Wang W, Vijayakumar M, Nie Z, Chen B, et al. A stable vanadium redox-flow battery with high energy density for large-scale energy storage. *Adv Energy Mater* 2011;1:394–400.
- Leung P, Shah AA, Sanz L, Flox C, Morante JR, Xu Q, et al. Recent developments in organic redox flow batteries: a critical review. *J Power Sources* 2017;360:243–83.
- Chen R. Toward high-voltage, energy-dense, and durable aqueous organic redox flow batteries: role of the supporting electrolytes. *ChemElectroChem* 2019;6: 603–12.
- Hollas A, Wei X, Murugesan V, Nie Z, Li B, Reed D, et al. A biomimetic high-capacity phenazine-based anolyte for aqueous organic redox flow batteries. *Nat Energy* 2018;3:508–14.
- Wei X, Pan W, Duan W, Hollas A, Yang Z, Li B, et al. Materials and Systems for Organic Redox Flow Batteries: status and challenges. *ACS Energy Lett* 2017;2: 2187–204.
- Hu B, DeBruler C, Rhodes Z, Liu TL. Long-cycling aqueous organic redox flow battery (AORFB) toward sustainable and safe energy storage. *J Am Chem Soc* 2017; 139:1207–14.
- DeBruler C, Hu B, Moss J, Luo J, Liu TL. A sulfonate-functionalized Viologen enabling neutral cation exchange, aqueous organic redox flow batteries toward renewable energy storage. *ACS Energy Lett* 2018;3:663–8.
- Yu J, Zhao T-S, Pan D. Tuning the performance of aqueous organic redox flow batteries via first-principles calculations. *J Phys Chem Lett* 2020;11:10433–8.
- Hu B, Tang Y, Luo J, Grove G, Guo Y, Liu TL. Improved radical stability of viologen anolytes in aqueous organic redox flow batteries. *Chem Commun* 2018;54:6871–4.
- Huskinson B, Marshak MP, Suh C, Er S, Gerhardt MR, Galvin CJ, et al. A metal-free organic–inorganic aqueous flow battery. *Nature* 2014;505:195–8.
- voltstorage.com. VoltStorage. <http://voltstorage.com/> (accessed 11 January 2023).
- vflowtech.com. VFlow Tech. <https://www.vflowtech.com/> (accessed 11 January 2023).
- h2aec.com. H2 Inc. <http://www.h2aec.com/> (accessed 11 January 2023).
- Lee W, Park G, Kim Y, Chang D, Kwon Y. Nine watt – level aqueous organic redox flow battery stack using anthraquinone and vanadium as redox couple. *Chem Eng J* 2020;398:125610.
- Jia C, Liu J, Yan C. A significantly improved membrane for vanadium redox flow battery. *J Power Sources* 2010;195:4380–3.
- Ye J, Yuan D, Ding M, Long Y, Long T, Sun L, et al. A cost-effective nafion/lignin composite membrane with low vanadium ion permeation for high performance vanadium redox flow battery. *J Power Sources* 2021;482:229023.

- [53] Li J, Long J, Huang W, Xu W, Liu J, Luo H, et al. Novel branched sulfonated polyimide membrane with remarkable vanadium permeability resistance and proton selectivity for vanadium redox flow battery application. *Int J Hydrogen Energy* 2022;47:8883–91.
- [54] Li J, Liu J, Xu W, Long J, Huang W, Zhang Y, et al. Highly ion-selective sulfonated polyimide membranes with covalent self-crosslinking and branching structures for vanadium redox flow battery. *Chem Eng J* 2022;437:135414.
- [55] Liu X, Zhang H, Duan Y, Yuan Z, Li X. Effect of Electrolyte Additives on the Water Transfer Behavior for Alkaline Zinc–Iron Flow Batteries. *ACS Appl Mater Interfaces* 2020;12:51573–80.
- [56] Knehr KW, Kumbur EC. Role of convection and related effects on species crossover and capacity loss in vanadium redox flow batteries. *Electrochem Commun* 2012; 23:76–9.
- [57] Oldenburg FJ, Bon M, Perego D, Polino D, Laino T, Gubler L, et al. Revealing the role of phosphoric acid in all-vanadium redox flow batteries with DFT calculations and in situ analysis. *Phys Chem Chem Phys* 2018;20:23664–73.
- [58] Chang F, Hu C, Liu X, Liu L, Zhang J. Coulter dispersant as positive electrolyte additive for the vanadium redox flow battery. *Electrochim Acta* 2012;60:334–8.
- [59] Wang H, Sayed SY, Luber EJ, Olsen BC, Shirurkar SM, Venkatakrishnan S, et al. Redox flow batteries: how to determine electrochemical kinetic parameters. *ACS Nano* 2020;14:2575–84.